

On direct estimation of hardening exponent in crystal plasticity from the spherical indentation test*

H. Petryk[†], S. Stupkiewicz and S. Kucharski

Institute of Fundamental Technological Research (IPPT), Polish Academy of Sciences
Pawińskiego 5B, 02-106 Warsaw, Poland

Abstract

A novel methodology is proposed for estimating the strain hardening exponent of a metal single crystal directly from the spherical indentation test, without the need of solving the relevant inverse problem. The attention is focused on anisotropic piling-up and sinking-in that occur simultaneously in different directions, in contrast to the standard case of axial symmetry for isotropic materials. To correlate surface topography parameters with the value of material hardening exponent, a finite-element study of spherical indentation has been performed within a selected penetration depth range using a finite-strain crystal plasticity model. It is shown how the power-law hardening exponent can be estimated from the measured pile-up/sink-in pattern around the residual impression after indentation in a (001)-oriented fcc single crystal of a small initial yield stress. For this purpose, a new parameter of surface topography is defined as the normalized material volume displaced around the nominal contact zone, calculated by integration of the local residual height (positive or negative) over a centered circular ring. That indicator can be easily determined from an experimental topography map available in a digital form. Comparison is made with the estimates based on measurements of the contact area and the slope of the load–penetration depth curve in logarithmic coordinates. The proposed methodology is extended to estimation of the hardening exponent simultaneously with the initial yield stress when the latter is not negligible. Experimental verification for a Cu single crystal leads to promising conclusions.

Keywords: metal crystal; elastoplasticity; finite deformation; strain hardening; experimental identification.

*Published in *Int. J. Solids Struct.* 112, 209–221, 2017, doi:10.1016/j.ijsolstr.2016.09.025

[†]Corresponding author, email: hpetryk@ippt.pan.pl

1 Introduction

This paper develops a methodology for direct extraction of the strain hardening exponent from the spherical indentation test performed on single crystals of ductile metals. The major challenge is to avoid a typical but laborious identification procedure that involves numerical solving of the relevant inverse problem afterwards. Instead of that, we propose more straightforward estimation of that important plasticity parameter using only the numerical simulation data to be provided beforehand.

Indentation is a convenient method for quick estimation of mechanical properties of materials, especially at small (micro or nano) length scales when it is not easy to obtain bulk material samples suitable for other experimental testing methods. The standard purpose of indentation tests is to determine hardness and elastic stiffness modulus of the material. It is highly desirable but less straightforward to extend the scope and to use the information available from indentation tests for identification of plastic properties of a ductile material.

Early attempts of such identification from the spherical indentation (Brinell) tests were limited to empirical observations of macroscopically isotropic materials. Meyer (1908) has revealed that the mean contact pressure increases with the ratio of contact radius to ball diameter according to a power law. O’Neil (1944) has found that the relationship between stress and plastic strain for the indented material can be fitted by a power law with the same exponent n . Norbury and Samuel (1928) (see Alcala et al. (2000) for a more recent account) have observed that the hardening exponent n is correlated with the amount of pile-up or sink-in in vicinity of the residual impression. Tabor (1951) has summarized the earlier findings and formulated a linear relationship between the mean contact pressure beneath the indenter tip and the flow stress corresponding to a representative plastic strain.

A progress in the theory has been made by Hill et al. (1989) who provided a theoretical background for experimental observations mentioned above. They have proposed an analytic similarity solution of the spherical indentation problem formulated in specially scaled variables for a rigid-plastic material obeying a power-law potential. In particular, the current-to-nominal projected contact area ratio (known as c^2 parameter), that characterizes the degree of piling-up or sinking-in, has been found to remain constant during indentation and dependent in a specified manner on the power-law exponent n alone. Although the analytic solution neglects the initial yield stress and elasticity effects – especially at small indentation loads, cf. (Mesarovic and Fleck, 1999; Taljat and Pharr, 2004)) – and finite deformation effects (at higher loads), it has established a firm basis for further attempts to extract the material hardening curve from spherical indentation tests in cases when those effects are not substantial.

Many papers have been devoted to identification of parameters of elastic-plastic polycrystalline materials, usually treated as isotropic, from indentation tests. Based on finite

element simulations, corrections have been introduced to the fundamental formulae resulting from the rigid-plastic idealization of Hill et al. (1989), to take into account the effect of elastic deformation on the parameters measured in indentation experiments. The corrected formulae were next used in identification procedures (Francis, 1976; Field and Swain, 1995; Taljat et al., 1998; Kucharski and Mróz, 2001, 2004; Nayebi et al., 2002; Cao and Lu, 2004; Cao et al., 2007; Ogasawara et al., 2009). The information on pile-up or sink-in patterns, supplementary to that available from instrumented indentation load–depth curves, was also used for identification purposes by inverse analysis, e.g., (Bolzon et al., 2004; Lee et al., 2004; Bocciarelli et al., 2005). The above list of references is only exemplary, nevertheless, it can be concluded that extracting elastic-plastic material properties from indentation tests is a challenge till now, even in the case of isotropic materials.

In metal single crystals, the problem of identifying hardening parameters from indentation tests is additionally affected by crystallographic anisotropy. The plastic anisotropy is described by activity of a discrete number of crystallographic slip-systems governed in essence by the Schmid rule. While indentation tests performed on single crystals have been simulated in many papers by using the crystal plasticity theory (Wang et al., 2004; Liu et al., 2005, 2008; Alcalá et al., 2008; Casals and Forest, 2009; Chang et al., 2010; Zambaldi and Raabe, 2010; Eidel, 2011; Zambaldi et al., 2012; Kucharski et al., 2014; Alcalá et al., 2015; Renner et al., 2016), the problem of identification of material parameters used in such simulations is still open. Usually, a satisfactory agreement of numerical and experimental results has been obtained (Liu et al., 2008; Alcalá et al., 2008; Zambaldi and Raabe, 2010; Eidel, 2011; Zambaldi et al., 2012; Kucharski et al., 2014; Alcalá et al., 2015; Renner et al., 2016) by selecting suitable crystal plasticity models and their parameters to fit the known experimental data. However, it is desirable to have a procedure for direct estimation of some basic strain-hardening parameters of an anisotropic single crystal of a ductile metal of unknown properties without the need of solving any inverse problem, just by carrying out experimental indentation tests only and using the *existing* simulation data. Such a procedure is proposed in the present paper.

The isotropic part of the crystal hardening rule is typically separated from the anisotropic part described by the slip-system cross-hardening matrix, cf. (Peirce et al., 1982; Asaro, 1983). The isotropic hardening curve in the multislip case at moderate strains (stage III) can be expected to be governed approximately by the Voce law, cf. (Kocks and Mecking, 2003). However, the curvature of an initial part of that curve is described in the simplest way by a power-law hardening curve, within the usual tolerances. As noted by Saimoto (2006), during tensile deformation, [001] oriented crystals in Cu and Al do not strictly manifest a linear Stage II but a slightly non-linear one with a power-law exponent being about 0.8. The exponent need not be the same in the multislip case during compression. Of course, a single hardening parameter cannot reflect the complexity of the actual dislocation interactions, cf. (Kubin et al., 2008).

The major aim of this paper is to develop a methodology for estimating directly from indentation tests the power-law hardening exponent n for a virgin metal crystal of a low value of initial flow stress (of the order of 1 MPa). It is emphasized that exponent n is treated here as a basic parameter of the material in a certain range of plastic strain. The methodology is based on spherical indentation in an fcc single crystal along with measurements of the residual pile-up/sink-in topography that is far from axial symmetry. A new quantitative indicator of the value of n is introduced as the normalized material *volume* displaced around the nominal (spherical) contact zone, calculated by integration of a local residual height (positive or negative) *over a centered circular ring*. The indicator represents an extension of the 2D pile-up or sink-in area in the axial crosssection of an axially symmetric impression for an isotropic material to a generic 3D case for an anisotropic crystal when a single axial cross-section is no longer adequate. The proposed indicator can be determined, using an easily programmable subroutine, from an experimental topography map in a digital form which is commonly available nowadays. It can be regarded as an alternative to a more standard parameter, namely, the current-to-nominal projected contact area ratio, which is also investigated below but whose accurate measurement in experiments may be less straightforward. To correlate surface topography parameters with the value of material hardening exponent n , a finite-element study of spherical indentation has been performed for different values of n and within a selected indentation depth range at finite deformation.

The second, related aim of this paper is to extend the above methodology developed for a virgin crystal to a more general case when the initial yield shear stress, τ_0 , is no longer negligible. In that case, identification of n is to be done jointly with τ_0 , the latter being normalized by the flow stress corresponding to a representative plastic strain. The basic concept of that two-parameter identification is presented below; a more detailed analysis is beyond the scope of this paper and will be presented elsewhere.

The final aim here is to verify the proposed procedure by predicting the uniaxial stress-strain curve and comparing it with an experimental one. For that purpose, one more parameter is needed that defines the stress magnitude. It is determined by adjusting the stress multiplier for each n so that the calculated load-penetration depth, $P-h$, curve in normalized coordinates $(h/R, P/R^2)$ goes through a representative experimental point $(h_{\text{exp}}/R_{\text{exp}}, P_{\text{exp}}/R_{\text{exp}}^2)$ in the indentation test for the crystal. Results of such verification are presented for a Cu single crystal.

It is pointed out that the plastic behaviour of a single crystal is examined here on the scale where size effects do not play an essential role (the penetration depth is above one micrometer). A separate problem, not covered in this paper, is the effect of strain gradients which are associated with creation of geometrically necessary dislocations and, consequently, can cause size-effects in indentation tests, cf. (Ashby, 1970; Nix and Gao, 1998; Faghihi and Voyiadjis, 2012; Kucharski et al., 2016). A study of size effects is beyond the scope of this work.

2 Crystal plasticity model for spherical indentation

2.1 Single-crystal plasticity model

Elastic-plastic finite deformation of a single crystal is here modeled using the well-known constitutive framework of crystal plasticity (Hill and Rice, 1972; Asaro, 1983), and the specific model employed in this work is briefly described below. The model has been intentionally simplified as much as possible so that, firstly, the indentation effects studied in the sequel are not influenced by the complex constitutive dependencies and, secondly, the number of parameters is minimized. It must be realized that indentation offers rather limited possibilities of estimating multiple unknown material parameters simultaneously. Therefore, we have chosen the commonly used power-law hardening exponent as a single basic parameter of a virgin metal crystal for estimation in a certain range of plastic strain. For similar reasons, equal hardening of all slip systems has been assumed since the description of more physical anisotropic latent hardening would require at least one more parameter to be involved.

As it is standard in crystal plasticity, a set of crystallographic slip systems is considered, and plastic slip on each system of index α is governed by the corresponding resolved shear stress τ_α (to be defined later). In the classical Schmid law, the slip system can be active only if the resolved shear stress τ_α reaches the corresponding threshold value τ_α^c governed by a hardening rule. Here we adopt a three-parameter power-hardening law,

$$\tau_\alpha^c = \tau^c = C(\Gamma_0 + \Gamma)^n, \quad \dot{\Gamma} = \sum_{\alpha=1}^N |\dot{\gamma}_\alpha|, \quad (1)$$

where $\Gamma = \int_0^t \dot{\Gamma} dt$ is the accumulated total plastic slip, and $\dot{\gamma}_\alpha$ denotes the slip rate on slip system α . The classical Taylor cross-hardening matrix has been assumed so that all slip systems harden equally, i.e. $\tau_\alpha^c = \tau^c$ for all α . Besides the power-law hardening exponent n that constitutes the main concern of this paper, the hardening law involves two other parameters, C and Γ_0 . It is convenient in the further discussion to replace C and Γ_0 with two out of three other related parameters, namely

$$\tau_0 = C\Gamma_0^n, \quad \tau_\# = C(\Gamma_0 + \Gamma_\#)^n, \quad \kappa = \tau_0/\tau_\#, \quad (2)$$

where τ_0 is the initial yield shear stress at $\Gamma = 0$ and $\tau_\#$ is the flow shear stress at $\Gamma = \Gamma_\#$, see Fig. 1. The choice of the reference value $\Gamma_\#$, to be fixed throughout the paper, is discussed in Section 2.2. We examine the case when all the above parameters are strictly positive. At fixed $\Gamma_\#$ and for a given value of n , parameter Γ_0 is in one-to-one correspondence to $\kappa = (1 + \Gamma_\#/ \Gamma_0)^{-n}$, and for given values of n and κ the stress multiplier $C = C_\#$ can be determined by specifying $\tau_\#$, cf. formula (12)₃. We note that a two-parameter hardening law corresponding to $\tau_0 = 0$ (and $\Gamma_0 = 0$) would be a reasonable choice for a virgin high-purity metal crystal. However, such a model would anyway require some regularization at $\Gamma = 0$ to avoid the resulting numerical singularity.

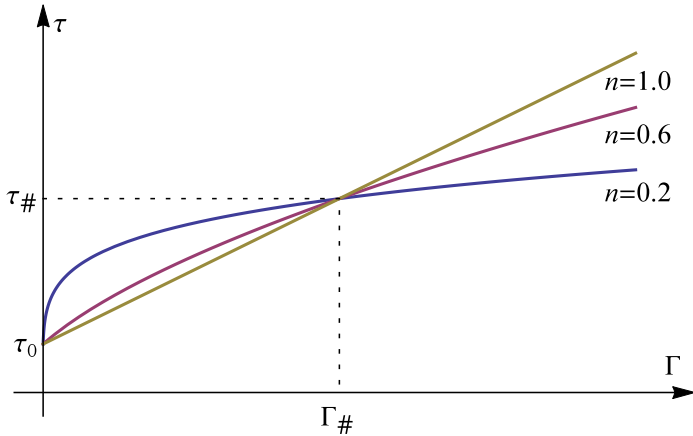


Figure 1: Parametrization of the power-law hardening curve.

A viscous-type kinetic equation is assumed to govern the slip rates $\dot{\gamma}_\alpha$,

$$\dot{\gamma}_\alpha = \frac{\dot{\lambda}}{\tau^c} \left(\frac{\tau_\alpha}{\tau^c} \right)^{2m-1}, \quad (3)$$

where $m \gg 1$ is an integer so that Eq. (3) holds for both positive and negative τ_α and $\dot{\gamma}_\alpha$. However, the plastic multiplier $\dot{\lambda} \geq 0$ is eliminated here by adopting a single yield condition (Arminjon, 1991; Gambin, 1992; Kowalczyk and Gambin, 2004) expressed in terms of the resolved shear stresses τ_α on all slip systems, $\alpha = 1, \dots, N$,

$$F = \left[\sum_{\alpha=1}^N \left(\frac{\tau_\alpha}{\tau^c} \right)^{2m} \right]^{1/(2m)} - 1 \leq 0. \quad (4)$$

This yield condition provides a regularization of the individual (Schmid) yield conditions $|\tau_\alpha| \leq \tau^c$, formulated for each slip system α , that are recovered in the limit as $m \rightarrow \infty$.

The finite strain formulation is based on the multiplicative decomposition of the deformation gradient \mathbf{F} into elastic part \mathbf{F}^e , which describes the lattice stretch and rotation, and plastic part \mathbf{F}^p ,

$$\mathbf{F} = \mathbf{F}^e \mathbf{F}^p, \quad \mathbf{C}^e = \mathbf{F}^{eT} \mathbf{F}^e, \quad \mathbf{L}^p = \dot{\mathbf{F}}^p \mathbf{F}^{p-1}. \quad (5)$$

The elastic right Cauchy–Green tensor \mathbf{C}^e and the plastic velocity gradient \mathbf{L}^p are defined accordingly, both in a locally unstressed, intermediate configuration of fixed lattice orientation. A superimposed mark -1 , T or $-T$ over a tensor symbol denotes an inverse, transpose or transposed inverse, respectively.

In view of small elastic strains, the anisotropic elastic response is simply described by assuming the St. Venant–Kirchhoff finite elasticity model formulated in the intermediate configuration,

$$\mathbf{S}^e = \mathbb{L} \mathbf{E}^e, \quad \mathbf{E}^e = \frac{1}{2} (\mathbf{C}^e - \mathbf{1}), \quad (6)$$

where \mathbf{S}^e is the corresponding second Piola–Kirchhoff stress tensor, and \mathbb{L} is a positive-definite, fourth-order tensor of elastic moduli.

Finally, the (generalized) resolved shear stress τ_α on slip system α is defined (Hill and Rice, 1972; Asaro, 1983) in terms of the Mandel stress tensor \mathbf{M} as follows:

$$\tau_\alpha = \mathbf{M} \cdot (\mathbf{s}_\alpha \otimes \mathbf{n}_\alpha), \quad \mathbf{M} = \mathbf{C}^e \mathbf{S}^e = \mathbf{F}^{eT} \boldsymbol{\tau} \mathbf{F}^e, \quad (7)$$

where the unit vectors \mathbf{n}_α and \mathbf{s}_α specify, respectively, the slip-plane normal and the slip direction for slip system α , both in the intermediate configuration, and $\boldsymbol{\tau}$ is the Kirchhoff stress. Eq. (7) defines a finite-strain counterpart to the classical Schmid stress. With all the above definitions, it can be shown that the overall plastic deformation, expressed in terms of the plastic velocity gradient \mathbf{L}^p , is governed by a *rate-independent* associated flow rule of Mandel's type (Mandel, 1971),

$$\mathbf{L}^p = \dot{\lambda} \frac{\partial F}{\partial \mathbf{M}} = \sum_{\alpha=1}^N \dot{\gamma}_\alpha \mathbf{s}_\alpha \otimes \mathbf{n}_\alpha, \quad (8)$$

accompanied by the usual complementarity conditions: $\dot{\lambda} \geq 0$ and $\dot{\lambda} F = 0$. At the same time, \mathbf{L}^p is equal to the sum of shear-rate contributions of individual slip systems, which is typical for the crystal plasticity models.

2.2 Geometric and material parameters in spherical indentation

During the spherical indentation test, the indentation load P and penetration depth h increase from zero to maximum values P_{\max} and h_{\max} , respectively. Upon unloading from the turning point (P_{\max}, h_{\max}) , P decreases to zero and h to a residual value $h_{\text{res}} > 0$. The indenter is modeled as a rigid sphere of radius R . The *nominal* contact radius with the indented *half-space* is $a = \sqrt{h(2R - h)}$ by elementary geometry, and its values corresponding to h_{\max} and h_{res} are denoted by a_{\max} and a_{nom} , respectively (Fig. 2). The actual contact radius of the indenter with the deformed anisotropic crystal depends strongly on the in-plane direction and can differ substantially from its nominal value.

We will consider indentation in an fcc single crystal of a pure metal. Neglecting an easy-glide stage in compression, it is assumed that the crystal obeys the elastic-plastic constitutive relationships given in Section 2.1 with the power-hardening law (1) whose exponent is to be identified in the spherical indentation test. Since the representative amount of accumulated plastic strain under a spherical indenter is related to the ratio h_{res}/R , the identification of n from spherical indentation can concern a certain range of plastic strain only. For macroscopically isotropic polycrystals, the representative strain ε_r at the periphery of a contact zone has been estimated by the classical Tabor formula $\varepsilon_r = 0.2a_{\text{iso}}/R$ (Tabor, 1951), where a_{iso} is the radius of the contact area projected on the initial planar surface of the indented specimen. For anisotropic single crystals investigated here, the real projected contact area is far from being circular. However, the *nominal* contact area A_{nom} can still be determined from

$$A_{\text{nom}} = \pi a_{\text{nom}}^2, \quad a_{\text{nom}} = \sqrt{h_{\text{res}}(2R - h_{\text{res}})}, \quad (9)$$

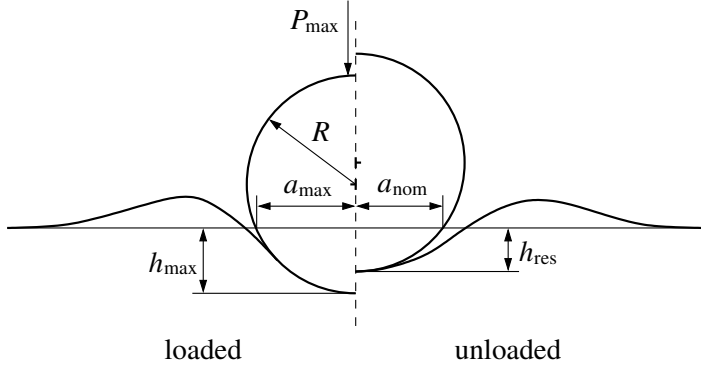


Figure 2: Geometrical parameters in spherical indentation: indenter radius R , maximum penetration depth h_{\max} at the maximum load P_{\max} , and the residual depth h_{res} after unloading. Nominal contact radii corresponding to h_{\max} and h_{res} are denoted by a_{\max} and a_{nom} , respectively. It is stressed that the actual impression topography is not axisymmetric due to crystal anisotropy.

so that, by elementary geometry, A_{nom} is the cross-section area of the spherical indenter cut by the initially planar surface of the material when the penetration depth equals to h_{res} .

In this paper, the attention is focused on spherical indentation in a (001)-oriented fcc single crystal up to a penetration depth from the range $0.01 \leq h_{\max}/R \leq 0.12$; study of other crystal orientations and penetration depths is postponed to a separate paper. For indentation in a ductile crystal in the fully plastic range, elastic springback effect is small and the residual depth can be expected to be close to h_{\max} . As no better estimate for single crystals is available at present, the Tabor formula with a_{nom} substituted in place of a_{iso} can be used to estimate roughly the strain range to which the estimated value of n might apply. This yields, for instance, $\varepsilon_r \approx 0.1$ for $h_{\text{res}}/R \approx 0.12$. Taking into account that for compression of an fcc crystal in [001] direction in the symmetric case the ratio of compressive logarithmic plastic strain ε to accumulated plastic shear Γ on all active $\{111\}\langle 0\bar{1}1\rangle$ slip-systems is equal to $\varepsilon/\Gamma = 1/\sqrt{6} \approx 0.408$, the identified value of n may be expected to correspond roughly to a value of $\Gamma \approx 0.23$ for $h_{\max}/R = 0.12$.

It is commonly known that virgin fcc single crystals of high-purity metals exhibit usually a very small value of the initial yield stress. As the initial yield stress τ_0 in the present elastic-plastic model cannot be taken equal to zero (cf. Section 2.1), we begin with assuming a low initial value of $\tau_0 = 1$ MPa and will examine the possibilities to identify the hardening exponent n from spherical indentation under this assumption. The effect of other values of τ_0 on the identified value of n will be studied afterwards.

Preliminary numerical studies have revealed that the value of indentation load corresponding to the selected maximum penetration depth $h_{\max}/R = 0.12$ depends for $\tau_0 = 1$ MPa only moderately on n if the shear stress τ is the same for different n at Γ of the order of 0.1 (i.e. at about a half of the value $\Gamma \approx 0.23$ mentioned above). This

has motivated our choice of the representative value of $\Gamma_{\#}$ in Eq. (2) as $\Gamma_{\#} = 0.1$, kept fixed throughout this paper. A realistic value of τ at $\Gamma = 0.1$ for a single crystal of pure Cu has been adopted as $\tau_{\#} = 40$ MPa. However, the numerical results to be expressed in non-dimensional quantities are not sensitive to the value of $\tau_{\#}$ but rather to the ratio $\kappa = \tau_0/\tau_{\#}$, and become precisely invariant with respect to proportional scaling of τ_0 and $\tau_{\#}$ at fixed $\Gamma_{\#}$ if the elastic moduli are also scaled accordingly.

In the numerical calculations reported on here, elasticity effects are calculated using the standard elastic constants corresponding to cubic anisotropy of Cu ($c_{11} = 170$ GPa, $c_{12} = 124$ GPa, $c_{44} = 75$ GPa), which corresponds to directional Young's modulus in the [001] direction $E_{[001]} = c_{11} - 2c_{12}^2/(c_{11} + c_{12}) \approx 65$ GPa. This gives $E_{[001]}/\tau_0 \approx 6.5 \cdot 10^4$ and $E_{[001]}/\tau_{\#} \approx 1.6 \cdot 10^3$, while $0.14 < a_{\max}/R < 0.5$ within the assumed range of $0.01 \leq h_{\max}/R \leq 0.12$. Hence, by analogy to the numerical results for isotropic materials (Mesarovic and Fleck, 1999; Taljat and Pharr, 2004), the surface deformation can be expected here to be dominated by plasticity and only slightly dependent on anisotropic elastic properties. It follows that the identification procedure proposed below, if verified positively for Cu, can be applicable to a wider spectrum of fcc metal crystals.

In accord with the present aim to keep the number of free factors as low as possible, frictionless contact is assumed in the present simulations of spherical indentation. It has been checked numerically that the effect of friction on the value of n estimated in Section 4 is not substantial.

2.3 Finite-element implementation

Simulations of spherical indentation, reported in Section 3, have been carried out using the finite element (FE) method. The computational model developed for that purpose is briefly described below.

The crystal plasticity model of Section 2.1 has been implemented in a displacement-based FE code. Incremental constitutive equations have been obtained by applying the implicit backward-Euler time integration scheme. In order to consistently treat plastic incompressibility, the incremental flow rule employs the exponential map integrator (Miehe, 1996; Steinmann and Stein, 1996). The resulting incremental equations are solved using the classical return-mapping algorithm (Simo and Hughes, 1998). This standard treatment is possible due to the regularization of the yield condition by Eq. (4).

However, for a large value of the regularization exponent m (the value of $m = 20$ has been used in the computations), the incremental equations become highly nonlinear which may cause convergence problems for the Newton method that is applied to solve to incremental constitutive equations. A robust algorithm has thus been developed by employing a kind of continuation method in which the exponent m is increased gradually from $m = 1$, and each intermediate converged solution is used as an initial guess for the Newton iterations corresponding to the subsequent increased value of m .

Computer implementation of the crystal plasticity model has been performed using *AceGen*, a code generation system that combines the symbolic algebra capabilities of *Mathematica* (www.wolfram.com) with an automatic differentiation (AD) technique and advanced expression optimization techniques (Korelc, 2002). Details concerning the related automation of FE code generation can be found in (Korelc, 2009; Korelc and Stupkiewicz, 2014).

In the present FE model, the spherical indenter is modeled as a rigid sphere, frictionless contact is assumed, and unilateral contact constraints are enforced using the augmented Lagrangian method (Alart and Curnier, 1991; Lengiewicz et al., 2011). The corresponding nodal Lagrange multipliers constitute the global unknowns, and the nonlinear FE equations are solved using the Newton method simultaneously with respect to all unknowns, i.e. displacements and Lagrange multipliers. The tangent operator required by the Newton method is obtained by exact linearization of the nonlinear FE equations, and this is achieved by applying the AD technique available in *AceGen*.

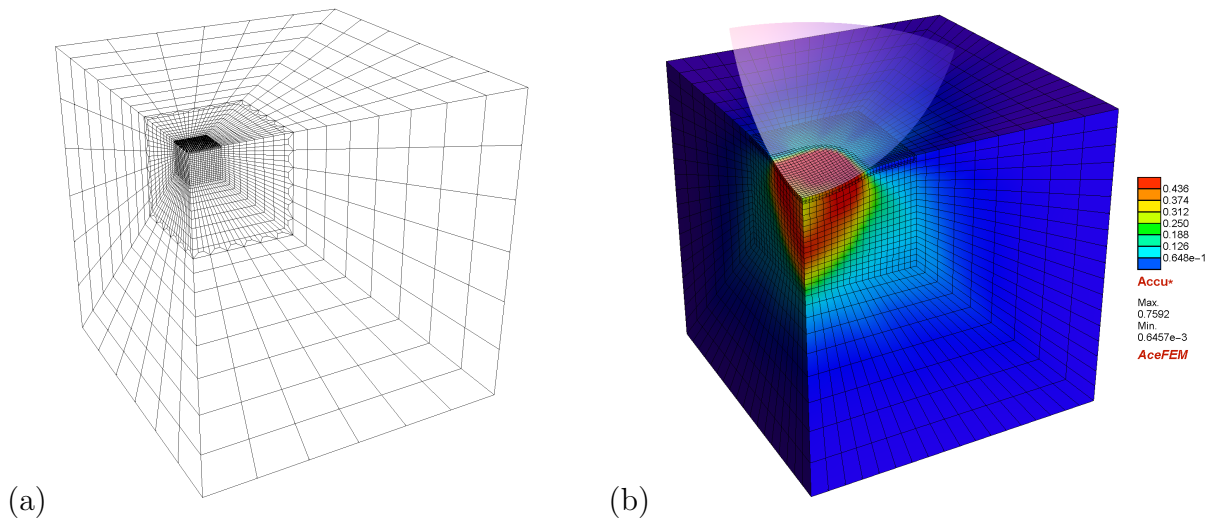


Figure 3: Spherical indentation in a (001)-oriented fcc crystal: (a) finite element mesh; (b) vicinity of the contact zone with the color map denoting the distribution of the accumulated total plastic slip Γ (the map corresponds to $h_{\max}/R = 0.12$, $n = 0.6$ and $\tau_0 = 1$ MPa).

The FE mesh used in the computations is shown in Fig. 3 along with a sample result of simulations where the calculated distribution of locally accumulated slip Γ on all slip systems is displayed. Spherical indentation of (001)-oriented fcc crystals is only considered, hence, by exploiting the related symmetry, the actual computational domain is reduced to one quarter of the problem. The size of the computational domain is set proportional to the maximal nominal contact radius $a_{\max} = \sqrt{h_{\max}(2R - h_{\max})}$, see Fig. 2. Specifically, the computational domain is a cube of the side length of $18a_{\max}$. The mesh is refined

towards the center of the contact zone (located at a vertex). The part of the contact surface with the finest mesh, where the actual contact occurs, is a square of the side length of $1.5a_{\max}$.

Hexahedral eight-node elements are used and the so-called F-bar formulation is employed in order to avoid volumetric locking effects (de Souza Neto et al., 1996). The computations are carried out using *AceFEM*, a flexible FE code that is integrated with *AceGen*.

3 Simulations of spherical indentation in fcc single crystal in [001] direction

3.1 Effects of the hardening exponent n

3.1.1 Indentation curve

The common result of an instrumented indentation test is the load–penetration depth (P – h) curve. The effect of the power-law hardening exponent n on the load–depth curve for spherical indentation into an fcc single crystal in [001] direction, simulated numerically for the material model described above for a small value of initial yield stress, $\tau_0 = 1$ MPa, is presented in Fig. 4. It can be seen that the curvature of the loading branch is correlated with n , although the differences are not significant. The possibility of identifying the value of n from logarithmic P – h plots will be discussed in more detail in Section 3.2. However, identification of n in that way may be not accurate, especially if the initial yield stress is not very small.

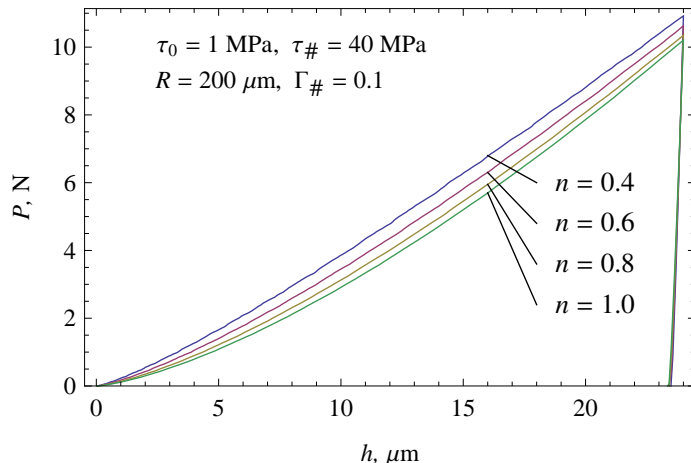


Figure 4: Load–penetration depth curves calculated for spherical indentation in fcc single crystal in [001] direction for different values of hardening exponent n , for a low value of the initial yield stress ($\kappa = \tau_0/\tau_{\#} = 0.025$).

The results shown in Fig. 4 and subsequent results reported for $\tau_0 = 1$ MPa correspond

to $n = 0.4, 0.6, 0.8, 1.0$. The results corresponding to $n = 0.2$ are not reported because the extremely high initial hardening rate at $\Gamma = 0$ for $n = 0.2$ requires regularization to avoid numerical problems, and this regularization makes the results visibly inconsistent with the remaining results. Actually, a minor regularization was needed also for $n = 0.4$, apparently introducing no visible inconsistency.

3.1.2 Pile-up and sink-in pattern after indentation

We focus now attention on the possibility of identifying the power-law hardening exponent from indentation tests by analysing the deformed surface topography. In the spherical indentation tests into isotropic (polycrystalline) ductile metals, the correlation between the power-law hardening exponent n and the pile-up or sink-in amount in the fully plastic range is well known (Norbury and Samuel, 1928; Hill et al., 1989; Alcalá et al., 2000). In turn, in the case of elastic-plastic indentation, numerical simulations have revealed that the amount of pile-up and sink-in depends not only on n but also on the penetration depth and ratio E/σ_y , where E and σ_y are, respectively, the elastic modulus and the yield stress of the material indented, cf. (Mesarovic and Fleck, 1999; Taljat and Pharr, 2004). Recently, Renner et al. (2016) have concluded, in agreement with Chang et al. (2010) and Zambaldi et al. (2012), that pile-up dimensions provide a very good strain-hardening indicator for a single crystal.

The correlation between the value of n and deformed surface topography is examined here in the case of anisotropic fcc single crystals of ductile metals of a small value of $\tau_0 = 1 \text{ MPa} = 0.025 \tau_{\#}$ and $0.01 \leq h_{\max}/R \leq 0.12$, with the intention to have a fully plastic range in vicinity of the indenter, cf. Section 2.2. The finite element simulations have been performed for different values of the hardening exponent n and different maximum penetration depths h_{\max} , the latter only slightly greater than the respective residual depths h_{res} found upon unloading. Resulting 3D maps of residual impressions for $n = 0.4, 0.6, 0.8, 1.0$ and $h_{\max}/R = 0.01, 0.02, 0.05, 0.12$ are shown in Fig. 5. The vertical range ($-0.1 \leq z/h_{\text{res}} \leq 0.1$) has been adjusted such that the pile-up and sink-in topography is shown in sufficient detail. The maps are thus cropped at the level of $z = -0.1 h_{\text{res}}$ so that the spherical part of the impression created by direct contact with the indenter is not visible.

The most important qualitative observation of the results shown in Fig. 5 is that the surface topography after indentation:

- (i) *depends strongly on the hardening exponent n* , showing less piling-up and more sinking-in with increasing n , and
- (ii) only slightly depends on the maximum penetration depth h_{\max} in the range $0.01 \div 0.12 R$ for a small value of $\kappa = \tau_0/\tau_{\#} = 0.025$.

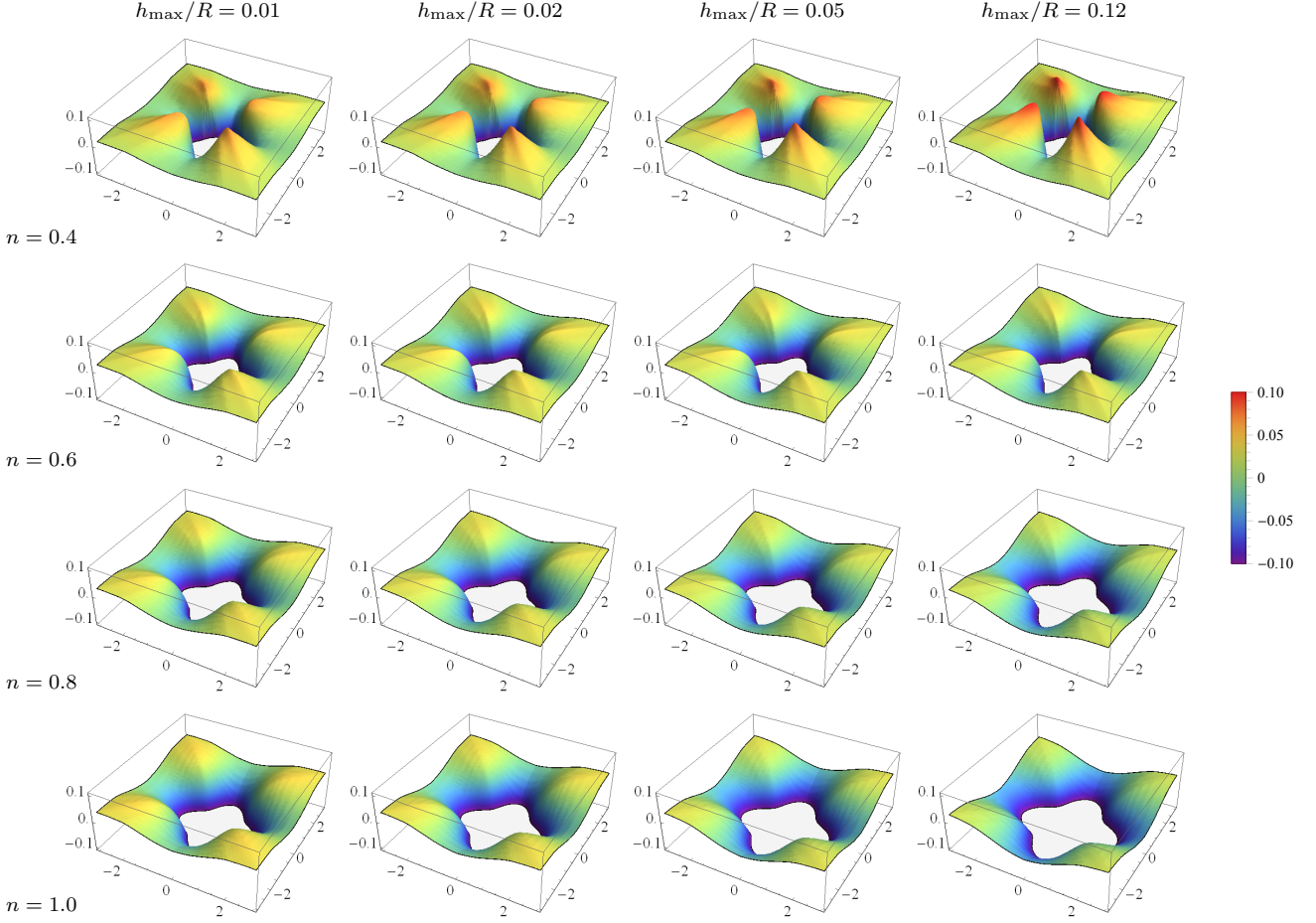


Figure 5: Maps of residual impressions after spherical indentation in an elastic-plastic fcc crystal in $[001]$ direction up to maximum penetration depth $h_{\max}/R = 0.01, 0.02, 0.05$ and 0.12 , calculated for the hardening exponent $n = 0.4, 0.6, 0.8$ and 1.0 and $\kappa = \tau_0/\tau_{\#} = 0.025$. The in-plane (horizontal) position is normalized by the nominal residual radius a_{nom} , while the pile-up (positive) and sink-in (negative) height is normalized by the residual depth h_{res} . In all cases the normalized maps are shown within the box $[-3, 3] \times [-3, 3] \times [-0.1, 0.1]$, and the color scale is used to visualize the normalized height $z/h_{\text{res}} \in [-0.1, 0.1]$.

The tendency (i) is also visualized in Fig. 6 which shows a top view of the residual impressions from the last column of Fig. 5 corresponding to $h_{\max}/R = 0.12$. The tendency (i) is to some extent qualitatively similar to the well-known effect of the hardening exponent on the pile-up/sink-in behaviour of an isotropic material, with the clear distinction that here the surface topography is far from being axisymmetric. The quantitative visualization of the observations (i) and (ii) shown in Figs. 5 and 6 for the anisotropic ductile crystal has not been found in the literature.

It can be concluded that, at least in the case of a small initial value of the flow stress, which is typical for virgin fcc single crystals of pure metals, just a quick look at

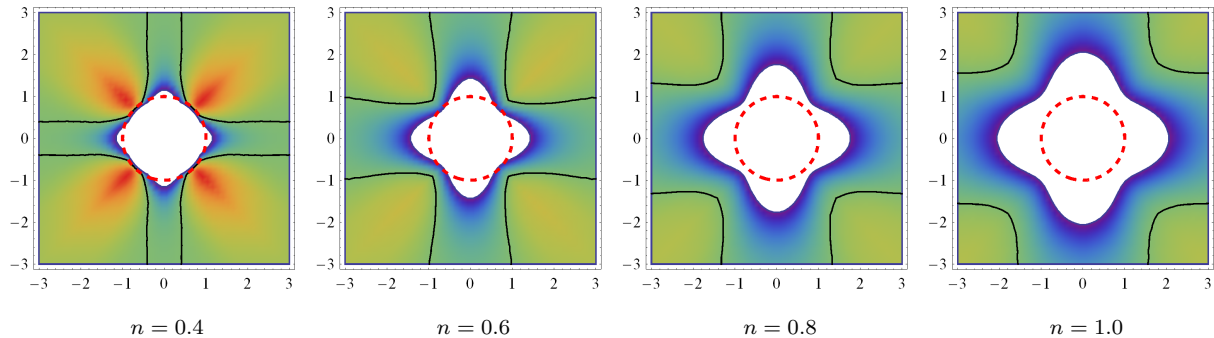


Figure 6: Top view of the residual impressions from the last column of Fig. 5 corresponding to $h_{\max}/R = 0.12$. Note the distinction between the material contour at the level of the initially planar surface (solid line) and the nominal contact area contour indicated by a central circle of radius a_{nom} (dashed line).

the experimental surface topography (cf. Fig. 14) after spherical indentation may be sufficient to extract a rough estimate of the value of n . For more refined estimation purposes, quantitative indicators can be used that are examined in the next section.

3.2 Hardening exponent indicators

3.2.1 Slope of indentation curve in logarithmic scale

In the rigid-plastic small-strain analysis of spherical indentation by Hill et al. (1989), a power-hardening law for the material with an exponent n corresponds to a power-type expression with an exponent $1 + \frac{n}{2}$ for the indentation load as a function of the increasing penetration depth. It is natural to check whether plastic anisotropy, a low but finite initial yield stress, elasticity and finite deformation effects do not destroy that power-type relationship.

The results of FE simulations of the spherical indentation test in [001] direction for $\tau_0 = 1$ MPa are shown in Fig. 7 as the double logarithmic plots of P - h relationships for the loading branch, expressed in the normalized variables taken as the ratios of the current to maximum values. A least-squares fit to each of the sequences of numerical points calculated in the range $0.01 \leq h_{\max}/R \leq 0.12$ for the material hardening exponent $n = 0.4, 0.6, 0.8$ and 1.0 , by Hill's et al. (1989) analytic relationship

$$\frac{P}{P_{\max}} = \left(\frac{h}{h_{\max}} \right)^{1 + \frac{n_p}{2}} \quad (10)$$

with one adjustable parameter n_p , is also shown in the figure. It can be seen that the power-type fit is quite good, in spite of the effects of elasticity and finite deformation taken into account in the FE simulations. However, the fitting values of n_p for the numerical P - h curves deviate from the values of n assumed for the material in the simulations,

especially for higher n . Moreover, the numerical plots are rather close to each other, so that the accuracy of identification of n from those plots may be not satisfactory.

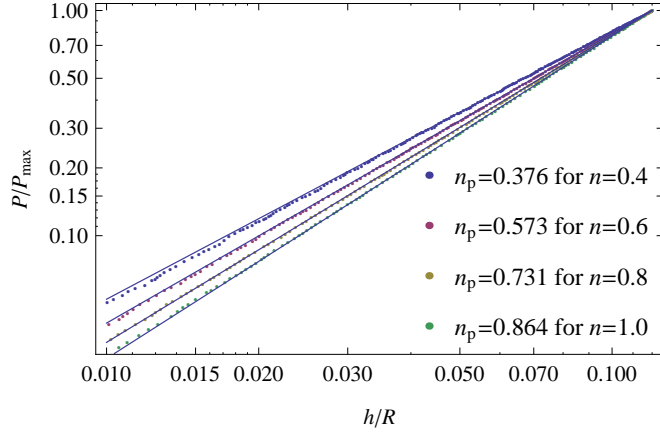


Figure 7: Double logarithmic point plots in normalized coordinates of the numerical P – h relationships for the loading branch in spherical indentation in fcc single crystal for different values of n and a low initial yield stress $\tau_0 = 1$ MPa. Analytic fits according to Eq. (10) are displayed by solid lines.

If the initial yield stress τ_0 is higher, e.g., for a prestressed crystal, then the numerical plots analogous to those shown in Fig. 7 become still closer to each other, and their slope depends on the initial yield stress as well as on h/R . Such plots are omitted here as it is hard to identify from them the actual hardening exponent.

3.2.2 Contact area

The value of contact area is one of the basic indentation-test parameters required to determine the fundamental material characteristics like hardness and Young’s modulus. An approximate value of the contact area in spherical indentation is provided by its nominal value defined by formula (9), frequently simplified further by neglecting the subtracted term h_{res} as a small fraction of $2R$. The actual-to-nominal contact area ratio, known as c^2 parameter, is most commonly used as a measure of pile-up or sink-in amount correlated with the value of hardening exponent n in axially symmetric cases (Norbury and Samuel, 1928; Hill et al., 1989; Alcalá et al., 2000). The question thus arises whether an analogous correlation exists in case of spherical indentation into ductile single crystals where the pile-up/sink-in behaviour is much more complex and far from axial symmetry.

The present numerical simulations provide an affirmative answer in case of a small value of initial yield stress. From the FE computations, it is known which material elements have been in contact with the indenter at the maximum load, therefore it is straightforward to determine the respective contact area and its projection A on the initial planar surface of the indented material.

The results of finite element simulations for $\tau_0 = 1$ MPa and different values of the hardening exponent n are shown in Fig. 8. As expected from the general correlation of the pile-up/sink-in pattern with the hardening exponent n visible in Fig. 5, there is a strong dependence of the value of the actual-to-nominal contact area ratio A/A_{nom} on n , while the dependence of the ratio A/A_{nom} on the residual penetration depth h_{res} is only slight.

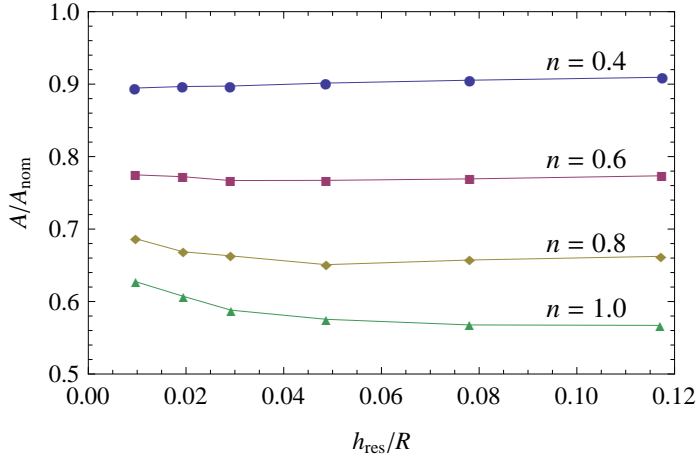


Figure 8: Projected contact area A vs residual depth h_{res} normalized by nominal contact area A_{nom} and indenter radius R , respectively. The markers indicate numerical results calculated for spherical indentation in fcc single crystal in [001] direction for $\kappa = 0.025$ and different values of hardening exponent n .

In principle, just one value of experimental contact area A measured after spherical indentation up to a penetration depth from the range $0.05 \leq h_{\text{max}}/R \leq 0.12$, say, suffices for approximate identification of hardening exponent n for the indented metal crystal. This can be done by comparing the experimental value of A/A_{nom} with that obtained by linear interpolation between the flat portions of the plots in Fig. 8. The so-extracted value of n is associated with a given value of the ratio $\kappa = \tau_0/\tau_{\#}$. The diagram in Fig. 8, although calculated for a low value of $\kappa = 0.025$, still changes slightly if τ_0 is reduced further at fixed $\tau_{\#} = 40$ MPa. For instance, if τ_0 is reduced to a (rather unrealistic) value of 0.01 MPa then the minimum value of the ratio A/A_{nom} found for $n = 1$ (linear hardening) decreases by 11% to 0.507, closely to the theoretical Hertz value of 0.5 for linear isotropic elasticity and to the numerical value of 0.508 obtained by Hill et al. (1989) for an isotropic rigid-linearly hardening solid.

There are some difficulties in using A/A_{nom} as the hardening exponent indicator. In spite of mesh refinement in the contact zone, the effect of FE discretization of the contact surface on A has not yet been fully eliminated, which can be seen from certain irregularities of the plots in Fig. 8. Irregularities appeared as more pronounced for higher values of κ , therefore the related results are not presented here. On the other hand, experimental measurements of the real contact area may also be not straightforward.

Those difficulties motivated the search for another indicator that would be less sensitive to contact area determination. A new quantitative indicator for identification of n from pile-up/sink-in behaviour in spherical indentation tests is proposed below.

3.2.3 Ring-based pile-up/sink-in volume

From Fig. 5 it can be observed that the higher n the less pronounced piling-up and the more pronounced sinking-in in respective sectors around the central depression. This suggests that the total volume (taken positive for piling-up and negative for sinking-in) of the material displaced around the area pushed down directly by the indenter can serve as a good indicator of the value of n . After a number of trials, it is proposed, as the best indicator from those examined, to calculate the volume described above as an integral of a local residual height (positive or negative) over a centered circular ring of internal radius a_{nom} and external radius $2a_{\text{nom}}$. The internal radius has been chosen equal to a_{nom} in order to eliminate from the ring-based volume the depression enforced directly by contact with the indenter. The external radius of $2a_{\text{nom}}$ has been selected more arbitrarily as a possibly optimal value for diminishing sensitivity of the ring-based volume to factors other than the plastic properties of the material, for instance, to imperfections inevitable in experiment. No clear reason has been found for complicating the simplest integer multipliers (1, 2) of the proposed radii (a_{nom} , $2a_{\text{nom}}$). Finally, the volume calculated as above, denoted by $V_{\text{ring}}[a, 2a]$, is normalized by the (positive) volume $V_{\text{cap}}[0, a]$ of the spherical segment (cap) of the indenter beneath the nominal planar surface when the penetration depth is equal to the residual depth h_{res} .

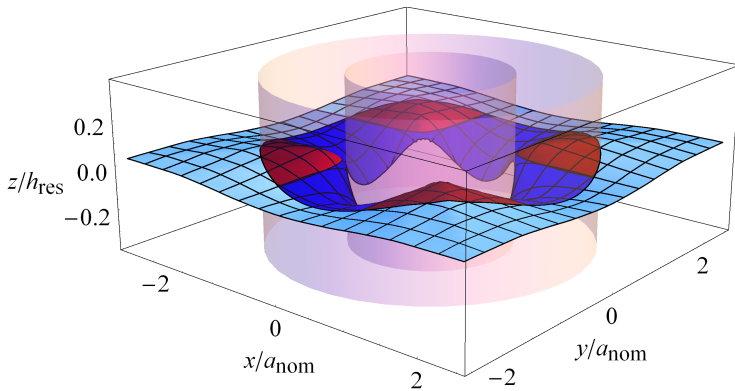


Figure 9: Illustration of the ring-based pile-up/sink-in volume V_{ring} . The red and blue parts of the residual impression surface denote, respectively, the positive (pile-up) and negative (sink-in) regions within the ring-based hollow cylinder that contribute to the \bar{V}_{ring} parameter defined by Eq. (11).

To summarize, we propose to use as the indicator of n after spherical indentation the

following normalized ring-based pile-up/sink-in volume:

$$\bar{V}_{\text{ring}} = \frac{V_{\text{ring}}[a, 2a]}{V_{\text{cap}}[0, a]}, \quad V_{\text{ring}}[a, 2a] = \int_a^{2a} \int_0^{2\pi} z(r, \varphi) r \, d\varphi \, dr, \quad (11)$$

calculated in cylindrical coordinates (r, φ, z) using the surface $z(r, \varphi)$ formed by material points lying initially on the planar surface $z = 0$ of the indented material, where $V_{\text{cap}}[0, a] = \pi h_{\text{res}}^2 (R - h_{\text{res}}/3)$ by elementary geometry. The proposal is illustrated in Fig. 9.

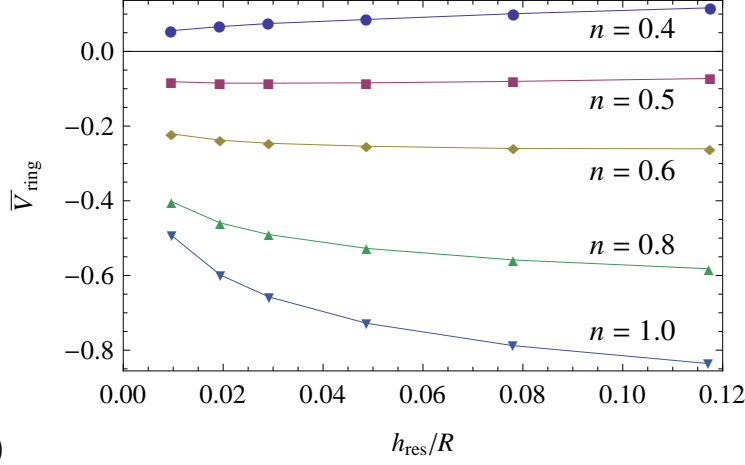
The value of \bar{V}_{ring} can be determined in a straightforward manner from a digitized map of the impression, which nowadays is easily available, from both FE simulations and experimental measurements.

The results of FE simulations performed for three different values of the initial yield stress τ_0 and for the displayed range of the hardening exponent n and penetration depth are presented in Fig. 10.

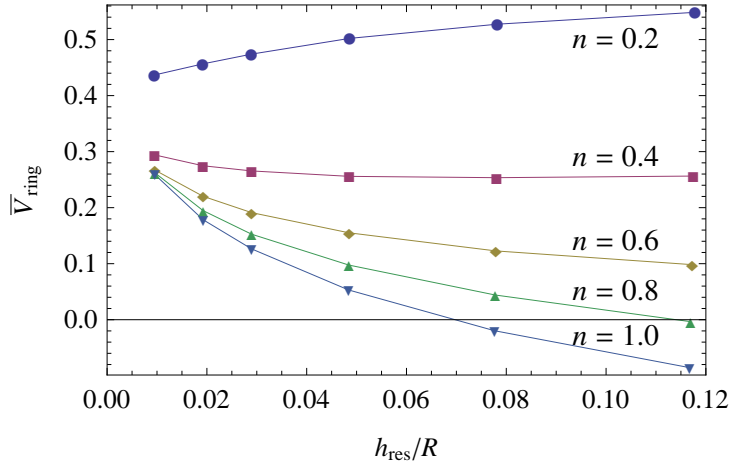
Several interesting conclusions can be drawn from Fig. 10. Let us discuss first the case of small initial yield stress $\tau_0 = 1$ MPa presented in Fig. 10a (recall that $\tau_{\#} = 40$ MPa at $\Gamma_{\#} = 0.1$ has been adopted in all calculations). A strong correlation exists between the values of \bar{V}_{ring} indicator and hardening exponent n in case of spherical indentation into a single crystal of a small initial yield stress corresponding to $\kappa = 0.025$. Hence, for τ_0 of that order, identification of the value of n from Fig. 10a alone is straightforward (by interpolation) if just one value of \bar{V}_{ring} is known for some h_{res}/R , and such n is only slightly dependent on the indentation depth h_{res} from the range $0.05 \leq h_{\text{res}}/R \leq 0.12$, say. The influence of smaller values of h_{res}/R on \bar{V}_{ring} becomes more essential for $n > 0.6$.

The situation changes for higher values of κ as shown in Figs. 10b and c. The effect of h_{res}/R on \bar{V}_{ring} is no longer negligible, while the sensitivity of \bar{V}_{ring} to n decreases significantly as the indentation depth decreases to $h_{\text{res}}/R = 0.01$. Figure 10 provides thus the possibility of extracting at least the order of magnitude of the initial yield stress from the value of \bar{V}_{ring} obtained from the spherical indentation experiment performed to a penetration depth $h_{\text{res}}/R \approx 0.01$.

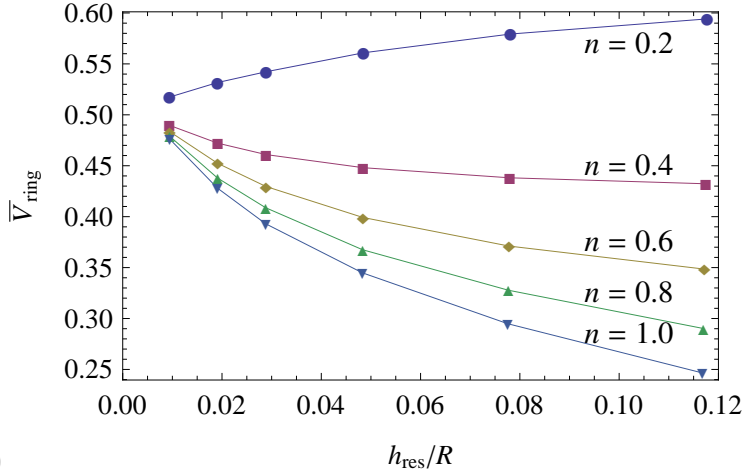
An important general conclusion is that the value of hardening exponent n can be identified with a good accuracy only if the ratio $\kappa = \tau_0/\tau_{\#}$ is given or estimated simultaneously with n . As the ranges of \bar{V}_{ring} in Figs. 10a,b,c only partially overlap, especially at small penetration depths, the provided \bar{V}_{ring} plots versus h_{res}/R for different n and κ offer the possibility to identify roughly, by interpolation, an unknown *pair* (n, κ) from several values of \bar{V}_{ring} determined experimentally for different depths h_{res}/R . The identification would be more accurate from \bar{V}_{ring} diagrams for a more dense spectrum of values of κ , but our first task is to verify the proposed identification procedure experimentally. Such an experimental verification by spherical indentation in a pure copper crystal is presented below.



(a)



(b)



(c)

Figure 10: The ring-based pile-up/sink-in volume parameter \bar{V}_{ring} versus the residual depth h_{res} normalized by indenter radius R . \bar{V}_{ring} is defined by formula (11) as the normalized total pile-up (positive) and sink-in (negative) volume over the ring of radii $[a_{\text{nom}}, 2a_{\text{nom}}]$ on the nominal planar surface. The markers indicate numerical results calculated for spherical indentation in fcc single crystal in $[001]$ direction for different values of hardening exponent n , for (a) $\kappa = 0.025$, (b) $\kappa = 0.25$, (c) $\kappa = 0.5$.

4 Experimental estimation of n

4.1 Experimental procedure

The spherical indentation tests have been performed on (001)-oriented high-purity copper single crystals. The CSM Open Platform equipment has been used to perform the indentation tests. The MHT micro-indenter was applied in micro-scale to measure load–penetration depth curves. The displacement resolution and load resolution are 0.3 nm and 100 μN , respectively, and the radius of the applied tip was nominally 200 μm and effectively $R_{\text{exp}} = 190 \mu\text{m}$ for $h > 10 \mu\text{m}$. The range of maximum loads was 0.25–11 N, and the load was applied in the quasi-static regime. To measure the deformed surface topography in the microscale, the scanning profilometer (Hommel-Etamic T8000 Nanoscan) was used, of vertical resolution less than 1 nm and lateral resolution of 0.1 μm and 0.5 μm in x - and y -direction, respectively.

High-purity (99.9999%) Cu single crystals, produced by the Czochralski method, were acquired from MaTecK GmbH (Germany). The crystals were cut into samples by spark erosion and wire saw to give a (001)-oriented planar surface. The surface was mechanically polished, then electro-polished, and finally carefully cleaned with distilled water and isopropyl alcohol. Next, a number of micro-indentation tests were performed. To be sure that the hardened surface layer generated in the polishing process is removed, electro-polishing and cleaning were repeated until the load–penetration depth curves were consistent in two subsequent steps.

4.2 Estimation of n for a virgin Cu single crystal

4.2.1 Indentation curves

From a series of spherical indentation tests performed on virgin (as-received) Cu single crystals, two representative experimental P – h point plots for the loading branch have been selected; other experimental P – h curves have been found to lie within that range. The two plots are shown in Fig. 11 in normalized coordinates in log–log scale and compared to the fitting lines from Fig. 7. The linear character of the experimental log–log relationship can readily be seen. By fitting the formula (10) using the two experimental data point sets, the extracted values of n_p are 0.414 and 0.472. Next, by linear interpolation between the closest fitting lines shown in Fig. 11, the respective values of the hardening exponent n_{exp} estimated in that way from the spherical indentation experiment are $0.44 \div 0.50$.

It is emphasized that the solid lines in Fig. 11 and thus the above identification of n refer to the low value of $\tau_0 = 1 \text{ MPa}$ used in the FE simulations. This order of τ_0 is consistent with the experiment performed on a virgin Cu single crystal, see Section 4.4. Nevertheless, as already mentioned in Section 3.2.1, the accuracy of identification of n from P – h plots alone may be not satisfactory.

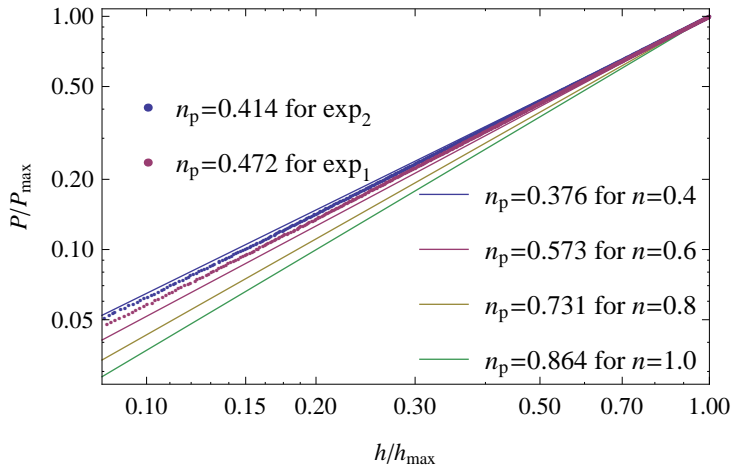


Figure 11: Double logarithmic plots of two representative experimental P - h curves for spherical indentation, expressed in non-dimensionalized variables and compared to the fitting lines from Fig. 7.

4.2.2 Contact area

While in numerical simulations the maximal contact area can be calculated directly (within an approximation due to FE discretization of the contact surface), determining it from experiments is less straightforward.

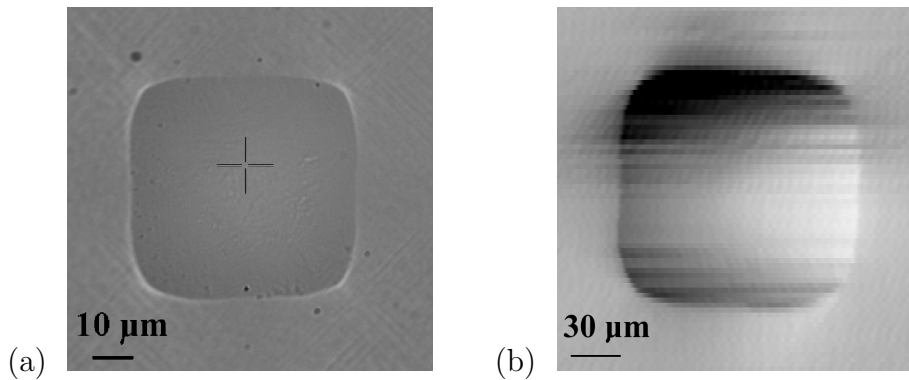


Figure 12: Top view of the projected contact area after spherical indentation in a (001)-oriented virgin Cu single crystal for (a) $h_{\text{res}} = 4.1 \mu\text{m}$ (optical micrograph), (b) $h_{\text{res}} = 21.7 \mu\text{m}$ (micrograph simulated from measured 3D topography).

The surface topography generated in spherical indentation tests in single crystals is rather complex, as in the same impression both pile-up and sink-in sectors occur, and consequently the contact radius depends strongly on the direction. The main problem in determination of contact area from experiments is in proper identification of the contact boundary on the residual impressions. In the investigations reported here, two approaches were applied: optical microscopy and scanning profilometry. We have observed that for shallow impressions, the contact boundary is sufficiently distinct in an optical micrograph,

Fig. 12a. At greater loads, when the height of pile-up is important, the depth of focus in the optical microscope was not sufficient to show the whole boundary distinctly. Then, the exact scan of impressions was made and the commercial software *Hommel Map* was applied to generate the acquired images. Next, the “photo simulation” option of *Hommel Map* was used for imaging the residual impression, Fig. 12b. In such an image, the contact boundary can be clearly seen and the projected area can be measured.

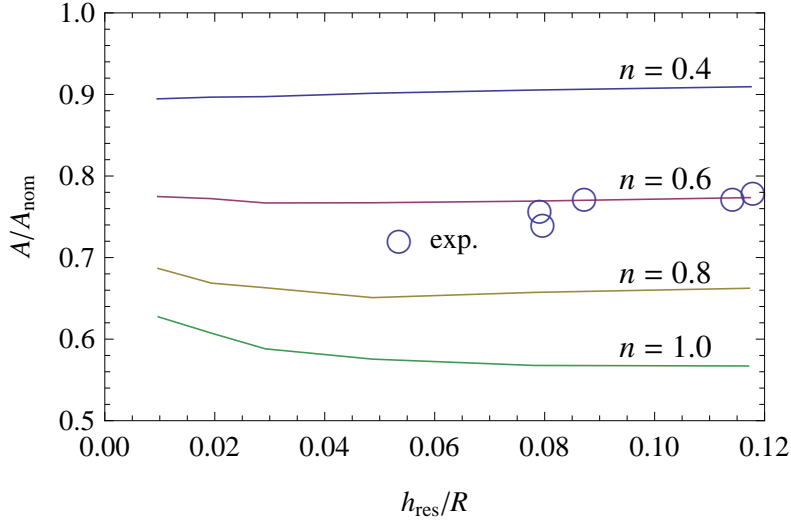


Figure 13: Projected contact area A vs residual depth h_{res} normalized by nominal contact area A_{nom} and indenter radius R , respectively. Experimental results for spherical indentation in a (001)-oriented virgin Cu single crystal are marked by circles and compared with numerical results from Fig. 8.

Figure 13 shows the comparison of the experimental area values for spherical indentation in a virgin Cu single crystal with the numerical results from Fig. 8 obtained for $\tau_0 = 1$ MPa. It can be seen that the value of n identified from the experimental contact area in the spherical indentation tests within the penetration depth range $h_{\text{res}}/R_{\text{exp}} = 0.08 \div 0.12$ is $n_{\text{exp}} \approx 0.6$. It becomes somewhat higher for smaller penetration depths (corresponding to a smaller effective strain for which n is identified). However, the values measured in the latter range were less accurate as the real indenter radius was found to be not constant near the indenter tip. Therefore, those values have not been used for identification purposes.

4.2.3 Ring-based pile-up/sink-in volume

The experimentally observed pile-up and sink-in patterns after indentation to different penetration depths h_{res} in the range between 10 and 22 μm are visually very similar to each other, as shown in Fig. 14. This is consistent with the slight dependence of surface topography on the value of penetration depth in the numerical simulations visualized in Fig. 5, and confirms the possibility of identifying the value of n using the surface

topography. Actually, by visual inspection, the experimental pile-up/sink-in patterns of Fig. 14 are found to be very similar to those numerical patterns of Fig. 5 that correspond to $n = 0.6$. Below, the volume-based parameter \bar{V}_{ring} is used for a quantitative and more objective assessment of this similarity.

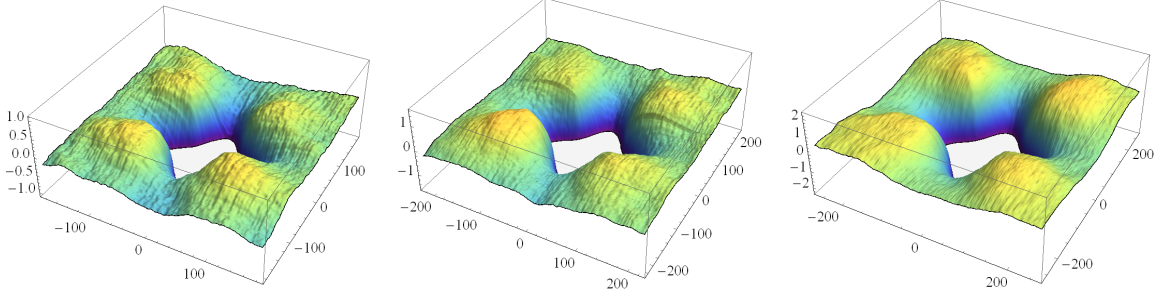


Figure 14: Experimental pile-up and sink-in patterns after spherical indentation in a (001)-oriented virgin Cu single crystal up to the penetration depths $h_{\text{res}} \approx 10, 15$ and $22 \mu\text{m}$ (from left to right; all dimensions are given in μm). For consistency with Fig. 5, the horizontal range is set to $\pm 3a_{\text{nom}}$ and the vertical range is set to $\pm 0.1h_{\text{res}}$.

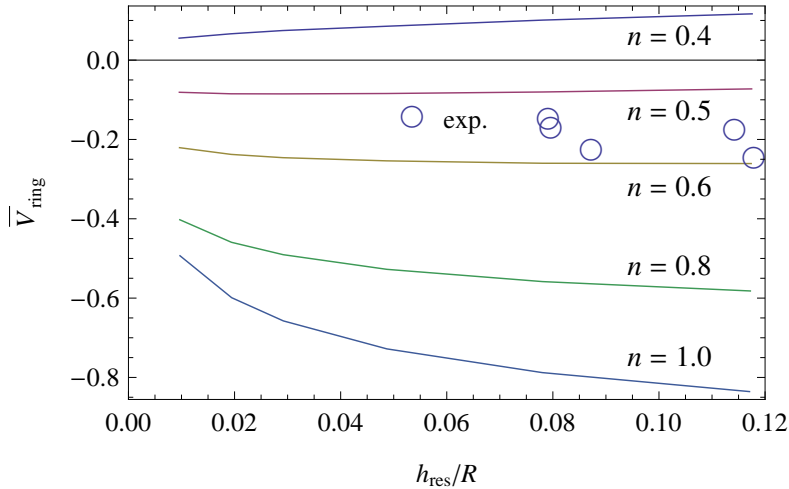


Figure 15: The ring-based pile-up/sink-in volume parameter \bar{V}_{ring} versus the residual penetration depth normalized by indenter radius R . Experimental results for spherical indentation in a virgin Cu single crystal are marked by circles and compared with numerical results from Fig. 10a.

Figure 14 has been generated from digital 3D maps of residual impressions, cf. Section 4.1. By relatively straightforward post-processing of those maps, respective values of the pile-up and sink-in volume indicator defined by Eq. (11) have been determined. The comparison to simulation results from Fig. 10 is shown in Fig. 15. The experimental points for $0.05 < h_{\text{res}}/R < 0.12$ lie in the range of $0.5 < n < 0.6$; values of \bar{V}_{ring} for

smaller h_{res} are not shown as they are somewhat less reliable in view of the deviations in geometry of the real indenter tip from a perfect sphere, as mentioned earlier. The value of n identified from the experimental values of the pile-up/sink-in volume indicator in the spherical indentation tests within the penetration depth range $h_{\text{res}}/R = 0.05 \div 0.12$ is thus $n_{\text{exp}} = 0.55 \pm 0.05$. It is in satisfactory agreement with $n_{\text{exp}} \approx 0.6$ from the contact area estimations and lies somewhat above the range $0.44 \div 0.50$ determined from the load–depth curves in logarithmic coordinates, all for a virgin Cu single crystal.

4.3 Estimation of n for a prestressed Cu single crystal

When a metal crystal is examined not in a virgin state but after a certain prestrain which significantly increases the initial dislocation density, the initial yield stress after prestrain is not negligible in comparison to the flow stress level at further strain of the order of $\Gamma_{\#} = 0.1$. Accordingly, a power-law hardening curve starting from zero stress after prestrain no longer provides a good approximation of the actual material behaviour.

From the analysis of simulation results presented in Section 3, it has been found that, for a crystal with a non-negligible initial yield stress, the pile-up/sink-in volume indicator \bar{V}_{ring} can provide better chances to identify the hardening exponent than the other two indicators (the slope of logarithmic P – h plots and the contact area) examined for spherical indentation. The experimental values of \bar{V}_{ring} determined from the spherical indentation tests performed as in Section 4.2 but on the crystal subjected first to compressive prestress of 38 MPa in [001] direction are of the order of $\bar{V}_{\text{ring}} \approx +0.2$. Those values do not fit the range of the numerical diagrams in Fig. 10 neither for $\kappa = 0.025$ nor for $\kappa = 0.5$, but fit the mid diagram for $\kappa = 0.25$, as shown in Fig. 16. More refined identification would require calculations performed for intermediate values of κ which have not yet been examined.

The mean value of n identified from Fig. 16 for the prestressed crystal is $n_{\text{exp}} \approx 0.5 \pm 0.1$, keeping in mind that the associated value of $\kappa = 0.25$ is identified here only roughly. Nevertheless, the value of $n_{\text{exp}} \approx 0.5 \pm 0.1$ for the prestressed crystal is in agreement with $n_{\text{exp}} \approx 0.55 \pm 0.05$ for the same but virgin crystal. More precise identification would require reliable experimental values of \bar{V}_{ring} for smaller values $h_{\text{res}}/R \approx 0.01$ and also numerical diagrams of \bar{V}_{ring} for intermediate values of κ , which is left for future study.

4.4 Verification by simple compression test

Finally, it is of primary interest to check whether the value of n_{exp} identified from spherical indentation provides good description of the experimental stress–strain curve.

In the FE computations, the constitutive multiplier C in formula (1) was adjusted using formulae (2) to a given ratio $\kappa = \tau_0/\tau_{\#}$ by taking the value of $\tau_{\#}$ prescribed arbitrarily as $\tau_{\#} = 40$ MPa. For identification of n alone, it is the value of the ratio $\kappa = \tau_0/\tau_{\#}$ that is essential, as discussed in detail above. In turn, for the purpose of predicting the complete stress–strain curve for the material, the value of C is to be

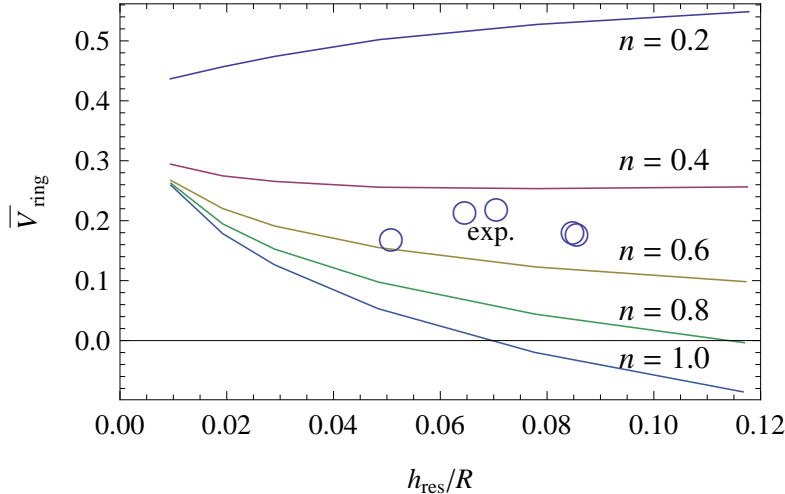


Figure 16: The ring-based pile-up/sink-in volume parameter \bar{V}_{ring} versus the residual penetration depth normalized by indenter radius R . Experimental results for spherical indentation in a prestressed Cu single crystal in $[001]$ direction are marked by circles and compared with numerical results from Fig. 10b for $\kappa = 0.25$.

identified from experimental indentation data. This is done by adjusting now the value of C in formula (1) for each n so that the calculated P - h curve in normalized coordinates $(h/R, P/R^2)$ goes through a representative experimental point $(h_{\text{exp}}/R_{\text{exp}}, P_{\text{exp}}/R_{\text{exp}}^2)$ in the indentation test for the crystal. Explicitly, the resulting parameter C is

$$C := r C_{\#}, \quad r = \frac{P_{\text{exp}}}{P(h_{\text{exp}}/R_{\text{exp}})} \frac{R^2}{R_{\text{exp}}^2}, \quad C_{\#} = \kappa \tau_{\#} \left(\frac{\kappa^{-\frac{1}{n}} - 1}{\Gamma_{\#}} \right) \quad (12)$$

for given n and κ , where the numerical function $P(h/R)$ for the prescribed pair $(\Gamma_{\#} = 0.1, \tau_{\#} = 40 \text{ MPa})$ and $\kappa = 0.025$ can be read off from the plots in Fig. 4 for each given n . From Eqs. (2) for prescribed $\Gamma_{\#}$ it follows that the value of Γ_0 is independent of the scaling by r , while the above scaling by r applies also to $\tau_0 := r\tau_0$ and $\tau_{\#} := r\tau_{\#}$. The effect of the related scaling of elastic constants by r is here negligible, which has been confirmed by additional FE computations (not reported here).

The representative values taken from the indentation tests reported on above are $h_{\text{exp}} = 22.7 \mu\text{m}$, $P_{\text{exp}} = 7.9 \text{ N}$ for the virgin Cu crystal, and $h_{\text{exp}} = 17.0 \mu\text{m}$, $P_{\text{exp}} = 7.3 \text{ N}$ for the prestressed Cu crystal (in each case $R_{\text{exp}} = 190 \mu\text{m}$). Clearly, in the assumed absence of an intrinsic characteristic length of the material, for the purposes of identification of the stress-strain curve neither h_{exp} nor R_{exp} need to be close to the values used in numerical calculations, only their ratio $h_{\text{exp}}/R_{\text{exp}}$ matters.

The comparison of the predicted and experimental uniaxial true stress-true strain curves in $[001]$ direction for the virgin and prestressed Cu single crystals is shown in Figs. 17 and 18, respectively. The predicted curves correspond to a theoretical elastic-plastic response, whose plastic part is governed by the (non-regularized) Schmid rule and hardening law (1) and (2) with the scaling factor r found from Eq. (12), and elastic

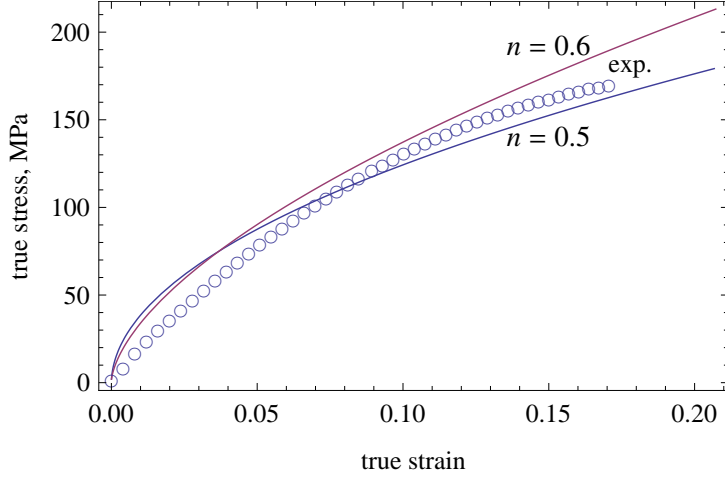


Figure 17: Comparison of the experimental uniaxial true stress–true strain curve for compression of a virgin Cu crystal in [001] direction with theoretical curves predicted for two values of n extracted from Figs. 13 and 15 and corresponding to $\kappa = 0.025$. The stress magnitude has been adjusted for each n according to Eq. (12).

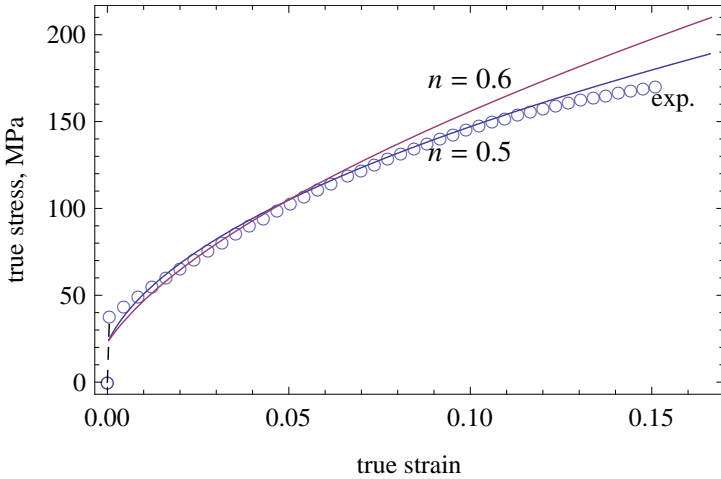


Figure 18: Diagram analogous to Fig. 17 but for a Cu crystal prestressed to 38 MPa in uniaxial compression in [001] direction. The theoretical curves correspond to $\kappa = \tau_0/\tau_{\#} = 0.25$.

response is defined by $E_{[001]}$. The experimental stress–strain curve in Fig. 17 was obtained by compressing a $5 \times 5 \times 10$ mm virgin crystal sample between flat steel platens (a PTFE tape and a molybdenum disulfide-based solid lubricant were used to reduce friction). The experimental curve in Fig. 18 has been reproduced from that in Fig. 17 for a virgin crystal by shifting it horizontally by the plastic prestrain of 0.021 corresponding to the prestress of 38 MPa.

From Fig. 17 it is clear that the experimental stress–strain curve, as it might be expected, does not follow precisely the power-law hardening for any constant n in the examined range. In turn, in Fig. 18 it is visible that the value of the initial yield stress

adopted is somewhat too small. Nevertheless, the agreement in both cases can be regarded as satisfactory within the strain range correlated to the maximum penetration depth $h_{\max} \approx 0.12 R$, cf. the discussion in Section 2.2. This also shows that the simple constitutive assumptions adopted in Section 2.1 are apparently adequate for the present purposes. Clearly, if the value of n is needed as a material parameter corresponding to a wider strain range then a higher penetration depth should be applied.

If the theoretical stress–strain curves shown in Figs. 17 and 18 are replaced with the numerical ones corresponding to the FE model used then the stresses are reduced by $\sim 5\%$ for $m = 20$ due to the regularization involved in the single yield condition (4). While this reduction would slightly improve the agreement with the experimental stress–strain curves, it is related to an unfavorable feature of the adopted viscous-type regularization (3) which implies that eight slip systems are simultaneously active during uniaxial compression along the high-symmetry [001] direction. In reality, the number of simultaneously active slip systems is expected to be lower due to the latent hardening effect. For instance, this is predicted by the incremental energy minimization treatment of rate-independent multislip in non-regularized crystal plasticity (Petryk and Kurska, 2013, 2015), whose application to FE simulations of spherical indentation is not attempted here.

5 Conclusion

A novel procedure has been developed for estimation of the power-law hardening exponent of an anisotropic fcc single crystal from the spherical indentation test, with the focus on residual pile-up/sink-in topography and without the need of solving the relevant inverse problem afterwards. The procedure is based on the results of the finite-element study of spherical indentation in an elastic-plastic fcc single crystal. Three indicators of the hardening exponent have been examined in detail. Respective diagrams have been provided for a (001)-oriented crystal within the penetration depth range $h_{\text{res}}/R = 0.01 \div 0.12$. They enable direct estimation of the hardening exponent n corresponding roughly to the value of the accumulated plastic shear up to $\Gamma \approx 0.23$ for that penetration depth range. This can be done by measurements of these indicators after carrying out the experimental test(s) of spherical indentation, without the necessity of performing further numerical simulations.

The finite element simulations have shown that, in qualitative terms, the influence of the hardening exponent on spherical indentation characteristics is to some extent similar to that observed in the case of isotropic materials. Specifically, with increasing n , the curvature of the loading branch of the load–penetration depth curve increases, the contact area decreases, and the overall pile-up volume decreases. This is described quantitatively by the respective three indicators examined. Unlike in the isotropic case, these indicators of n take fully into account the complex residual surface topography with distinct pile-up and sink-in sectors formed simultaneously around the central spherical depression.

A new indicator of hardening exponent n has been elaborated as the normalized pile-up/sink-in volume calculated by integration of the local residual height (positive or negative) over a centered circular ring. This indicator has turned out to be also useful for estimating the normalized initial yields stress from the indicator values for smaller penetration depths, and for extracting n subsequently from the indicator values measured for larger penetration depths from the examined range. If the initial yield stress is known to be sufficiently small then the diagrams provided for the more familiar indicators – the contact area and the slope of the load-depth curve in logarithmic coordinates – can also be used for extracting n , under certain reservations discussed earlier.

The identification procedure developed has been verified against experimental data obtained for a high-purity Cu single crystal. By adjusting the stress magnitude through a suitable fit of the experimental indentation load at a selected penetration depth, the complete hardening curve in the range of strains corresponding to spherical indentation has been predicted. Its agreement with the experimental stress–strain curve in uniaxial compression of a virgin Cu crystal has been found satisfactory. Finally, the estimation procedure has been applied to a prestressed Cu single crystal of a non-negligible initial yield stress, and consistent results have been obtained.

In the penetration depth range examined, the surface deformation was found to be dominated by plasticity and thus only slightly sensitive to the changes in material-dependent elastic moduli. Hence, the proposed estimation procedure may be applicable to a wider spectrum of fcc metal crystals, but confirmation of this hypothesis requires further study.

Acknowledgement The present research was partially supported by the Polish National Science Centre (NCN), grant NN 501 0672 40.

References

- P. Alart and A. Curnier. A mixed formulation for frictional contact problems prone to Newton like solution methods. *Comp. Meth. Appl. Mech. Engng.*, 92:353–375, 1991.
- J. Alcalá, A. C. Barone, and M. Anglada. The influence of plastic hardening on surface deformation modes around Vickers and spherical indents. *Acta Mater.*, 48:3451–3464, 2000.
- J. Alcalá, O. Casals, and J. Ocenasek. Micromechanics of pyramidal indentation in fcc metals: Single crystal plasticity finite element analysis. *J. Mech. Phys. Solids*, 56: 3277–3303, 2008.
- J. Alcalá, D. Esque-de los Ojos, and J. Ocenasek. Extracting uniaxial responses of single

- crystals from sharp and spherical hardness measurements. *Mech. Mater.*, 84:100–113, 2015.
- M. Arminjon. A regular form of the Schmid law. Application to the ambiguity problem. *Textures and Microstructures*, 14–18:1121–1128, 1991.
- R. J. Asaro. Micromechanics of crystals and polycrystals. *Adv. Appl. Mech.*, 23:1–115, 1983.
- M. F. Ashby. The deformation of plastically non-homogeneous materials. *Phil. Mag.*, 21: 399–424, 1970.
- M. Bocciarelli, G. Bolzon, and G. Maier. Parameter identification in anisotropic elasto-plasticity by indentation and imprint mapping. *Mech. Mater.*, 37:855–868, 2005.
- G. Bolzon, G. Maier, and M. Panico. Material model calibration by indentation, imprint mapping and inverse analysis. *Int. J. Sol. Struct.*, 41:2957–2975, 2004.
- Y. P. Cao and J. Lu. A new method to extract the plastic properties of metal materials from an instrumented spherical indentation loading curve. *Acta Mater.*, 52:4023–4032, 2004.
- Y. P. Cao, X. Qian, and N. Huber. Spherical indentation into elastoplastic materials: indentation-response based definitions of the representative strain. *Mater. Sci. Eng. A*, 454–455:1–13, 2007.
- P. Casals and S. Forest. Finite element crystal plasticity analysis of spherical indentation in bulk single crystals and coatings. *Comp. Mat. Sci.*, 45:774–782, 2009.
- H. J. Chang, M. Fivel, D. Rodney, and M. Verdier. Multiscale modelling of indentation in FCC metals: From atomic to continuum. *C. R. Physique*, 11:285–292, 2010.
- E. A. de Souza Neto, D. Perić, M. Dutko, and D. R. J. Owen. Design of simple low order finite elements for large strain analysis of nearly incompressible solids. *Int. J. Sol. Struct.*, 33:3277–3296, 1996.
- B. Eidel. Crystal plasticity finite-element analysis versus experimental results of pyramidal indentation into (001) fcc single crystal. *Acta Mater.*, 59:1761–1771, 2011.
- D. Faghihi and G. Z. Voyiadjis. Determination of nanoindentation size effects and variable material intrinsic length scale for body-centered cubic metals. *Mech. Mater.*, 44:189–211, 2012.
- J. S. Field and M. V. Swain. Determining the mechanical properties of small volumes of material from submicrometer spherical indentations. *J. Mater. Res.*, 10:101–112, 1995.

- H. A. Francis. Phenomenological analysis of plastic spherical indentation. *J. Eng. Mater. Technol.*, 98:272–281, 1976.
- W. Gambin. Refined analysis of elastic-plastic crystals. *Int. J. Sol. Struct.*, 29:2013–2021, 1992.
- R. Hill and J. R. Rice. Constitutive analysis of elastic-plastic crystals at arbitrary strain. *J. Mech. Phys. Solids*, 20:401–413, 1972.
- R. Hill, B. Storakers, and A. B. Zdunek. A theoretical study of the Brinell hardness test. *Proc. R. Soc. Lond.*, 423:301–330, 1989.
- U. F. Kocks and H. Mecking. Physics and phenomenology of strain hardening: the FCC case. *Progress Mater. Sci.*, 48:171–273, 2003.
- J. Korelc. Multi-language and multi-environment generation of nonlinear finite element codes. *Engineering with Computers*, 18:312–327, 2002.
- J. Korelc. Automation of primal and sensitivity analysis of transient coupled problems. *Comp. Mech.*, 44:631–649, 2009.
- J. Korelc and S. Stupkiewicz. Closed-form matrix exponential and its application in finite-strain plasticity. *Int. J. Num. Meth. Engng.*, 98:960–987, 2014.
- K Kowalczyk and W. Gambin. Model of plastic anisotropy evolution with texture-dependent yield surface. *Int. J. Plasticity*, 20:19–54, 2004.
- L. Kubin, B. Devincre, and T. Hoc. Modeling dislocation storage rates and mean free paths in face-centered cubic crystals. *Acta Mater.*, 56:6040–6049, 2008.
- S. Kucharski and Z. Mróz. Identification of plastic hardening parameters of metals from spherical indentation tests. *Mater. Sci. Eng. A*, 318:65–76, 2001.
- S. Kucharski and Z. Mróz. Identification of material parameters by means of compliance moduli in spherical indentation test. *Mater. Sci. Eng. A*, 379:448–456, 2004.
- S. Kucharski, S. Stupkiewicz, and H. Petryk. Surface pile-up patterns in indentation testing of Cu single crystals. *Exp. Mech.*, 54:957–969, 2014.
- S. Kucharski, D. Jarzabek, A. Piątkowska, and S. Woźniacka. Decrease of nano-hardness at ultra-low indentation depths in copper single crystal. *Exp. Mech.*, 56:381–393, 2016.
- Y. H. Lee, K. Takashima, Y. Higo, and D. Kwon. Prediction of stress directionality from pile-up morphology around remnant indentation. *Scripta Mater.*, 51:887–891, 2004.

- J. Lengiewicz, J. Korelc, and S. Stupkiewicz. Automation of finite element formulations for large deformation contact problems. *Int. J. Num. Meth. Engng.*, 85:1252–1279, 2011.
- Y. Liu, B. Wang, M. Yoshino, S. Roy, H. Lu, and R. Komanduri. Combined numerical simulation and nanoindentation for determining mechanical properties of single crystal copper at mesoscale. *J. Mech. Phys. Solids*, 53:2718–2741, 2005.
- Y. Liu, S. Varghese, J. Ma, M. Yoshino, H. Lu, and R. Komanduri. Orientation effects in nanoindentation of single crystal copper. *Int. J. Plast.*, 24:1990–2015, 2008.
- J. Mandel. *Plasticité classique et viscoplasticité*. CISM course No. 97. Springer, Wien, 1971.
- D. J. Mesarovic and N. A. Fleck. Spherical indentation of elastic-plastic solids. *Proc. R. Soc. Lond. A*, 455:2707–2728, 1999.
- E. Meyer. Untersuchungen über Härteprüfung und Härte. *Zeitschrift des Vereins deutschen Ingenieure*, 52:645–654, 1908.
- C. Miehe. Exponential map algorithm for stress updates in anisotropic multiplicative elastoplasticity for single crystals. *Int. J. Num. Meth. Engng.*, 39:3367–3390, 1996.
- A. Nayebi, R. E. Abdi, O. Bartier, and G. Mauvoisin. New procedure to determine steel mechanical parameters from the spherical indentation technique. *Mech. Mater.*, 34:243–254, 2002.
- W. D. Nix and H. Gao. Indentation size effects in crystalline materials: a law for strain gradient plasticity. *J. Mech. Phys. Solids*, 46:411–425, 1998.
- A. L. Norbury and T. Samuel. The recovery and sinking-in or piling-up of material in the Brinell test, and the effects of these factors on the correlation of the Brinell with certain other hardness tests. *J. Iron Steel Inst.*, 117:673, 1928.
- N. Ogasawara, N. Chiba, and X. Chen. A simple framework of spherical indentation for measuring elastoplastic properties. *Mech. Mater.*, 41:1025–1033, 2009.
- H. O’Neil. The significance of tensile and other mechanical test properties of metals. *Proc. Inst. Mech. Eng.*, 151:116, 1944.
- D. Peirce, R. J. Asaro, and A. Needleman. An analysis of nonuniform and localized deformation in ductile single crystals. *Acta Metall.*, 30:1087–1119, 1982.
- H. Petryk and M. Kurşa. The energy criterion for deformation banding in ductile single crystals. *J. Mech. Phys. Solids*, 61:1854–1875, 2013.

- H. Petryk and M. Kursa. Incremental work minimization algorithm for rate-independent plasticity of single crystals. *Int. J. Num. Meth. Engng.*, 104:157–184, 2015.
- E. Renner, Y. Gaillard, F. Richard, F. Amiot, and P. Delobelle. Sensitivity of the residual topography to single crystal plasticity parameters in Berkovich nanoindentation on FCC nickel. *Int. J. Plast.*, 77:118–140, 2016.
- S. Saimoto. Dynamic dislocation–defect analysis. *Phil. Mag.*, 86:4213–4233, 2006.
- J. C. Simo and T. J. R. Hughes. *Computational Inelasticity*. Springer-Verlag, New York, 1998.
- P. Steinmann and E. Stein. On the numerical treatment and analysis of finite deformation ductile single crystal plasticity. *Comp. Meth. Appl. Mech. Engng.*, 129:235–254, 1996.
- D. Tabor. *The hardness of metals*. Oxford Clarendon Press, 1951.
- B. Taljat and G. M. Pharr. Development of pile-up during spherical indentation of elastic–plastic solids. *Int. J. Sol. Struct.*, 41:3891–3904, 2004.
- B. Taljat, T. Zacharia, and F. Kosel. New analytical procedure to determine stress-strain curve from spherical indentation data. *Int. J. Sol. Struct.*, 35:4411–4426, 1998.
- Y. Wang, D. Raabe, C. Kluber, and F. Roters. Orientation dependence of nanoindentation pile-up patterns and of nanoindentation microtextures in copper single crystals. *Acta Mater.*, 52:2229–2238, 2004.
- C. Zambaldi and D. Raabe. Plastic anisotropy of c-TiAl revealed by axisymmetric indentation. *Acta Mater.*, 58:3516–3530, 2010.
- C. Zambaldi, Y. Yang, T. R. Bieler, and D. Raabe. Orientation informed nanoindentation of α -titanium: Indentation pileup in hexagonal metals deforming by prismatic slip. *J. Mater. Res.*, 27:356–367, 2012.